On the Assembly Bias of Cool Core Clusters Traced by Hα Nebulae

Elinor Medezinski[1] , Michael McDonald[2], Surhud More[3,4] , Hironao Miyatake[4,5,6], Nicholas Battaglia[7], Massimo Gaspari[1] , David Spergel[1,8], and Renyue Cen[1]

[1] Department of Astrophysical Sciences, 4 Ivy Lane, Princeton University, Princeton, NJ 08544, USA; elinorm@astro.princeton.edu.
[2] Kavli Institute for Astrophysics and Space Research, Massachusetts Institute of Technology, 77 Massachusetts Avenue, Cambridge, MA 02139, USA
[3] The Inter-University Center for Astronomy and Astrophysics, Post Bag 4, Ganeshkhind, Pune 411007, India
[4] Kavli Institute for the Physics and Mathematics of the Universe (WPI), Todai Institutes of Advanced Study, University of Tokyo, 5-1-5 Kashiwanoha, Kashiwa 277-8583, Japan
[5] Institute for Advanced Research, Nagoya University, Nagoya 464-8601, Aichi, Japan
[6] Division of Particle and Astrophysical Science, Graduate School of Science, Nagoya University, Nagoya 464-8602, Aichi, Japan
[7] Department of Astronomy, Cornell University, Ithaca, NY 14853, USA
[8] Center for Computational Astrophysics, Flatiron Institute, 162 5th Avenue, 10010, New York, NY, USA

Abstract

Do cool-core (CC) and non-cool-core (NCC) clusters live in different environments? We make novel use of Hα emission lines in the central galaxies of redMaPPer clusters as proxies to construct large (1000's) samples of CC and NCC clusters and measure their relative assembly bias using both clustering and weak lensing. We increase the statistical significance of the bias measurements from clustering by cross-correlating the clusters with an external galaxy redshift catalog from the Sloan Digital Sky Survey III, the LOWZ sample. Our cross-correlations can constrain assembly bias up to a statistical uncertainty of 6%. Given our Hα criteria for CC and NCC, we find no significant differences in their clustering amplitude. Interpreting this difference as the absence of halo assembly bias, our results rule out the possibility of having different large-scale (tens of Mpc) environments as the source of diversity observed in cluster cores. Combined with recent observations of the overall mild evolution of CC and NCC properties, such as central density and CC fraction, this would suggest that either the cooling properties of the cluster core are determined early on solely by the local (<200 kpc) gas properties at formation or that local merging leads to stochastic CC relaxation and disruption in a periodic way, preserving the average population properties over time. Studying the small-scale clustering in clusters at high redshift would help shed light on the exact scenario.

Key words: cosmology: observations – dark matter – galaxies: clusters: general – large-scale structure of universe

1. Introduction

In the modern picture of halo formation, clusters of galaxies, which are the last to collapse out of the large-scale structure (LSS) (Press & Schechter 1974), grow in an inside-out manner in two growth phases (Gunn & Gott 1972). In the early "fast-rate" phase, rapid matter accumulation and major merger events build up the internal core of the cluster inside a few times a characteristic scale radius ($r_s \approx 200$ kpc), erasing previous internal structure. In the subsequent "slow-rate" phase, the core is preserved, and the outskirts ($r > r_s$) gradually grow through moderate matter accretion. Thus, the internal structure of halos contains signatures of their growth history (Wechsler et al. 2002; Zhao et al. 2003; Ludlow et al. 2013; Correa et al. 2015). Whether the different baryonic properties of galaxy clusters are a product of the different assembly histories is a question worth investigating.

Interestingly, X-ray observations reveal that while on virial scales (~1 Mpc) clusters show remarkably self-similar entropy profiles as expected from hierarchical formation, their cores ($\lesssim 200$ kpc) show a significant departure from self-similarity, with a variety of cooling phases (Cavagnolo et al. 2009; McDonald et al. 2017, 2018). Cool-core (CC) clusters exhibit cuspy cores and low central temperatures and entropies (Cavagnolo et al. 2008, 2009; Hudson et al. 2010), whereas on the other end of the spectrum, non-cool-core (NCC) clusters have disturbed cores with flatter central densities and high core entropies (e.g., Ghirardini et al. 2019). The brightest cluster galaxies (BCGs) in CCs are often observed to coincide with a radio galaxy (e.g., McNamara & Nulsen 2007; Sun 2009; Hlavacek-Larrondo et al. 2015). A mechanical active galactic nuclei (AGN) feedback regulation has thus been invoked (see reviews by McNamara & Nulsen 2007, 2012; Fabian 2012; Gaspari 2015; McDonald et al. 2018) to explain lower than expected (~100–1000 $M_\odot$ yr^{-1}) star formation rates observed in the core (the "cooling-flow problem"; see Fabian 1994; O'Dea et al. 2008). Such an AGN regulation cycle should be tightly correlated with the ensemble warm/cold gas properties in CC clusters, such as high Hα/CO emission line luminosity and significant velocity dispersions (e.g., Donahue et al. 2000; Edge 2001; Salomé & Combes 2003; McDonald et al. 2010, 2012; Voit & Donahue 2015; Gaspari et al. 2018; Tremblay et al. 2018), indicative of recent or ongoing star formation.

The formation mechanism leading to these differences in cluster cores is still unclear. Following up Sunyaev–Zel'dovich (SZ) (Sunyaev & Zeldovich 1972) detected clusters in the X-ray with *Chandra*, McDonald et al. (2017) found little evolution of the gas properties in the cluster cores since $z \sim 1.6$, suggesting that the core thermal equilibrium is established early on and remains intact. Alternatively, transitions between CC and NCC may be periodic, that is, CCs are formed and destroyed quickly or in equal numbers, conserving a constant population over time. If the cores of clusters are indeed preserved over their lifetime, it would imply that only the initial local central gas density dictates the in situ formation (or lack thereof) of a central AGN and therefore the fate of the

cluster core. In that case, the large-scale environments of CCs should be indistinguishable from those of NCCs.

While high-resolution hydrodynamical simulations zooming in on the micro- to mesoscale (0.1–100 kpc) physics have been successful in unveiling the tight interplay between AGN feeding and feedback (e.g., Gaspari & Sądowski 2017; Yang et al. 2019), large-scale cosmological simulations (>1 Mpc) struggle to include all the key physics in a self-consistent manner needed to retain predictive power, leading to contrasting results depending on the chosen fine-tuned parameters (e.g., Rasia et al. 2015; Planelles et al. 2017; Barnes et al. 2018; Truong et al. 2018). As long as AGN feedback is implemented as a calibrated phenomenological subgrid model, robustly predicting the formation scenario of cluster cores in cosmological simulations will remain elusive.

In this case, can observations of galaxy clusters help us gain some insight into understanding the physical processes that dictate the centers of galaxy clusters? Dark matter halos are biased tracers of the underlying dark matter distribution (e.g., Kaiser 1984; White & Frenk 1991). This effect, especially on galaxy cluster scales, depends on halo mass to first order. The higher the mass, the larger the bias. However, at fixed mass, the assembly history of the dark matter halo plays a significant role in setting the halo bias (Sheth & Tormen 2004; Gao et al. 2005; Wechsler et al. 2006; Gao & White 2007; Li et al. 2008; Wang et al. 2011), with late forming halos being more biased than their early forming counterparts. Thus the differences in the halos' bias as manifested by their different clustering amplitudes could potentially be used as markers of assembly history in order to learn about the physical processes going on in galaxy clusters.

The assembly bias effect was first recognized in N-body simulations, whereby, for example, massive (>$10^{14}\,M_\odot$) halos that formed earlier showed lower clustering at fixed halo mass (Gao et al. 2005; Wechsler et al. 2006; Gao & White 2007; Wang et al. 2007). Parameters other than halo age were also found to correlate with clustering, such as concentration (Wechsler et al. 2006; Gao & White 2007; Faltenbacher & White 2010; Villarreal et al. 2017), spin (Gao & White 2007; Lacerna & Padilla 2012; Lazeyras et al. 2017), halo shape (Lazeyras et al. 2017; Villarreal et al. 2017), and the level of halo substructure (Wechsler et al. 2006; Gao & White 2007). Most of these secondary properties correlate strongly with assembly history; thus the effect was named assembly bias. However, the secondary parameters often also depend on the halo mass itself, making it hard to disentangle the two effects (Yang et al. 2006; Croton et al. 2007; Zentner et al. 2014; Salcedo et al. 2018). Partly for this reason, assembly bias has been hard to confirm observationally (Lin et al. 2016). It is only marginally detected on galaxy scales (Montero-Dorta et al. 2017; Niemiec et al. 2018), while on cluster scales, where the effect is predicted to be even weaker, observed results appear to suffer from selection biases (Miyatake et al. 2016; More et al. 2016; Busch & White 2017; Zu et al. 2017).

In Medezinski et al. (2017, hereafter M17), we developed a novel methodology to study the assembly bias of galaxy clusters. First, in order to increase the statistical power, instead of using the two-point auto-correlation function (ACF) of the clusters as is typically done, we instead cross-correlate each target cluster sample with a galaxy sample that probes the LSS with lower shot noise (see also More et al. 2016). Subsequently, by comparing the cluster-galaxy cross-correlation

function (CCF) around CC and NCC clusters, one can study the differences in the assembly histories of such galaxy clusters and potentially probe whether these two types of clusters are primordially distinct. In M17, we used the X-ray core entropy, a rather expensive observable that can only be resolved by the *Chandra* X-ray satellite, in order to separate the CC/NCC clusters. This restricted our sample size severely to only a few dozen clusters in each category. The measured bias therefore suffered from a statistical error larger than the expected level of assembly bias.

With the prevalence of wide-field optical imaging surveys such as the Sloan Digital Sky Survey (SDSS; Eisenstein et al. 2011), samples of thousands of clusters can now be used to study cluster evolution statistically (Soares-Santos et al. 2011; Szabo et al. 2011; Wen et al. 2012; Oguri 2014; Rykoff et al. 2014). To date, the most extensive public catalog applied to SDSS/Data Release 8 (DR8) imaging, the redMaPPer catalog (Rykoff et al. 2014, 2016), contains about 26,000 clusters. Furthermore, about a million of the brightest galaxies were spectroscopically followed up in SDSS/DR12, including most of redMaPPer's BCGs. As demonstrated by McDonald (2011), the signatures of cooling in a BCG spectrum can be used to distinguish between CC and NCC clusters and study their properties over significantly larger ensembles than ever before.

In this paper, we aim to leverage the statistical power of the redMaPPer cluster sample, exploit the cooling information provided by the BCG spectra, and apply the methodology developed in M17 to statistically determine whether CC and NCC clusters have different clustering properties and thus come from peaks collapsing from different initial conditions (i.e., assembly bias) or due to random processes (local in space and time) as indicated by the inside-out formation model (i.e., no assembly bias).

This paper is organized as follows. In Section 2 we present the observational data set used. In Section 3 we review how to derive the relative cluster bias from weak lensing (WL) and galaxy clustering. In Section 4 we present our results, utilizing WL to disentangle the mass bias effect and presenting the relative bias as measured from different lensing and clustering estimators. We discuss our results and compare with recent simulations in Section 5 and summarize and conclude in Section 6. Throughout the paper, we adopt a ΛCDM cosmological model, where $\Omega_m = 0.27$, $\Omega_\Lambda = 0.73$, and $h = H_0/100\,\mathrm{km\,s^{-1}\,Mpc^{-1}} = 1$. Unless otherwise stated, we quote median and 68% confidence interval values.

2. Data

Similar to the methodology presented in M17, our goal is to compare two subsamples of clusters that differ in their cooling state, having either cool or NCCs, and test whether they have different clustering amplitudes. To do so, we measure the clustering of galaxies as tracers of the LSS around each cluster subsample. The ratio of their clustering gives an estimate of their *relative* halo bias (see Section 3.1 for definitions). In this paper, we increase the statistical power of the method in M17 by using a larger sample drawn from the redMaPPer catalog and make novel use of the intensity of cooling lines in BCGs to differentiate between CC and NCC clusters. In the following section we describe the construction of the cluster subsamples and present the correlation between BCG emission line luminosity and cluster core entropy. We then briefly describe the galaxy catalog used for the cross-correlation study, LOWZ.
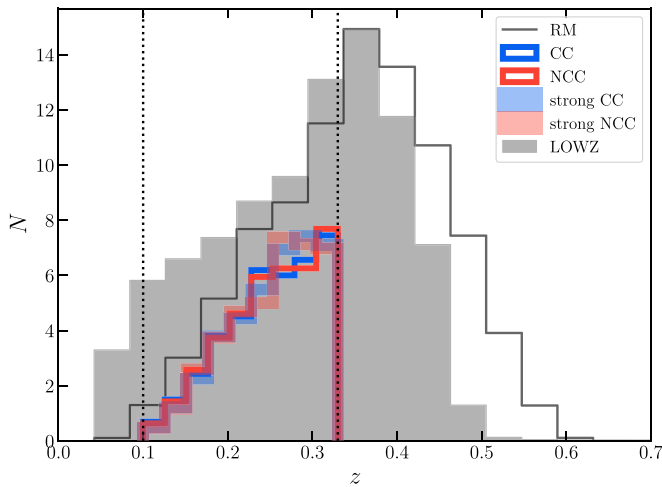
Figure 1. Redshift distribution of the different samples: the full parent cluster sample, redMaPPer (black line), CC and NCC samples (thick blue and red lines, respectively), strong CC and NCC (thin blue and red lines, respectively), and the LOWZ galaxy sample (gray). All samples have arbitrary normalization.

2.1. The redMaPPer Cluster Catalog

We use the latest optically selected galaxy cluster catalog detected from SDSS/DR8 with the redMaPPer cluster finder algorithm version 6.3 (Rykoff et al. 2014, 2016) available online.[9] For each cluster, the catalog lists redshift, richness estimate λ (approximately the number of cluster galaxies above $0.2 L_*$), and a position, where the position is that of the BCG. BCG identification in redMaPPer is good to 85% (Rozo & Rykoff 2014; Rykoff et al. 2014; Hoshino et al. 2015). This version of the catalog contains a total of 26,111 clusters detected in $\sim 10,000$ deg^2, spanning redshifts in the range $0.08 < z < 0.6$ and richnesses $\lambda > 20$. We present the redshift distribution of the full-cluster sample in Figure 1 (black), where throughout we use the spectroscopic redshift from SDSS (see item 3 in Section 2.1.1). A cluster random catalog (see footnote 9) has also been constructed (Rykoff et al. 2016), appropriate for large-scale two-point correlation studies such as the one conducted here. It is constructed to have the same richness and redshift distribution as the redMaPPer catalog. It has roughly $\times 100$ the size of the cluster catalog itself. However, for computation speed, we downsample it to have $\times 30$ the size of the CC/NCC subsamples (see definitions in Section 2.1.2), as those are much smaller than the full-cluster sample. We use weights provided in the random catalog to account for survey depth and redshift completeness. Since we aim to cross-correlate the clusters with the LOWZ galaxy catalog, both catalogs need to span the same spatial region on the sky. For LOWZ, some patches observed early on in the survey were masked due to a bug in the initial targeting software (see Reid et al. 2016). We therefore apply the LOWZ North and South masks onto the redMaPPer cluster and random catalogs. Finally, we confine our analysis to clusters within $0.1 < z < 0.33$ for an approximately volume-limited sample (Miyatake et al. 2016) and apply the same redshift limits to the random catalog.

2.1.1. Emission Line Luminosity as a CC Indicator

In order to determine whether a cluster is in CC or NCC phase, we search for signatures of cooling in the spectrum of its BCG. It has been shown that clusters that harbor multiphase gas with a cool gas core and low central entropy ($\lesssim 30$ keV cm^2) typically also exhibit strong emission line luminosities from Hα filaments of gas cooling onto their BCG (e.g., Cavagnolo et al. 2008; McDonald 2011; Gaspari et al. 2018). We therefore calculate Hα emission line luminosities for each redMaPPer BCG following these steps:

1. We query emission line fluxes from the emissionLine-sPort[10] table (Thomas et al. 2013) in SDSS/DR12 for all galaxies within the same redshift range as the clusters. Fluxes have been corrected for dust extinction where possible in the original data set provided by Thomas et al. (2013).

2. Where there are duplicate spectra per galaxy (i.e., measured by both SDSS and BOSS), we use the most recent one (BOSS).

3. We cross-match the redMaPPer catalog with the emission line table using the SDSS OBJID identifier. This provides emission line flux estimates (and spectroscopic redshift) for each cluster. About 17,000 (out of the 26,000) are left after this matching.

4. We remove entries where the continuum could not be fitted at the Hα location (i.e., Flux_-Cont_Ha_6562 $= -9999$ or Flux_-Cont_Ha_6562_Err $= 0$) or measured with low significance, signal-to-noise ratio (S/N) < 5.[11,12]

5. We convert flux to luminosity using the base cosmology and the BCG spectroscopic redshift.

6. For low-redshift galaxies ($z < 0.3$), the aperture size of the spectral fiber can be smaller than the galaxy size, causing the luminosity to be underestimated. Following McDonald (2011), we correct for this effect by assuming the total emission line luminosity does not evolve with redshift. We then fit a power-law model to the decreasing trend of the median luminosity as a function of redshift, L (z). Since the fiber size changed from $3''$ in the SDSS phase to $2''$ in the BOSS phase, we calculate the correction separately for SDSS and BOSS spectra (determined by the plate number).

In total, we are left with 6687 clusters with emission line information on their BCG in the redshift range $0.1 < z < 0.33$ with LOWZ spatial coverage. The main limiting factor is the redshift range we adopt.

We present the corrected Hα luminosity as a function of redshift in Figure 2 for all the BCGs in the redMaPPer sample. Many ($\sim 30\%$) BCGs have emission line luminosities below the tail of the distribution, $L_{H\alpha} \lesssim 10^{38}$ erg s^{-1}, with nearly all having no Hα detection (indicted as red upper limits in the figure).

Next we examine the correlation of emission-line luminosity with central entropy. We use the ACCEPT sample by Cavagnolo et al. (2009) who measured entropy profiles for

---

[9] http://risa.stanford.edu/redmapper/

[10] http://skyserver.sdss.org/dr12/en/help/browser/browser.aspx#&&history=description+emissionLinesPort+U

[11] S/N is defined as the continuum flux over its error measured at Hα, S/N = Flux_Cont_Ha_6562/Flux_Cont_Ha_6562_Err.

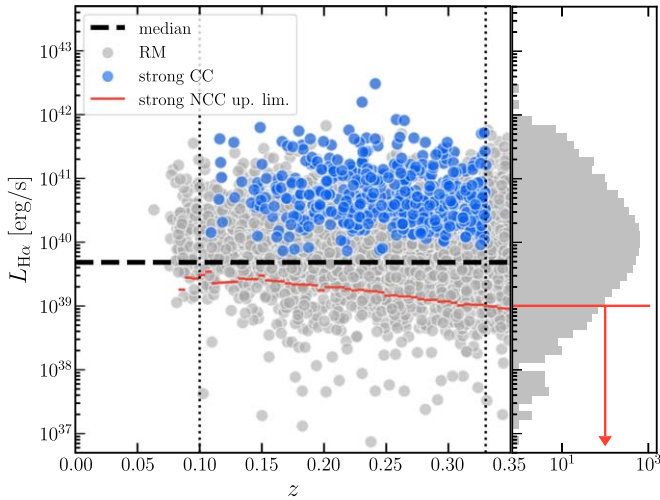[12] Only six clusters are removed by this cut. Most clusters have S/N > 60.

Figure 2. Hα luminosity for each redMaPPer BCG with robustly measured spectroscopy as a function of redshift. The redshift limits adopted are marked as vertical dotted lines. The dashed black line indicates the median luminosity of the sample (including nondetections), above (below) which clusters are considered CC (NCC) clusters. We also mark clusters that are considered strong CC (blue points), for which the Hα luminosity detection is significant (i.e., AoN > 2; see Section 2.1.2). Equivalently, those with null Hα emission lines are considered strong NCCs, and their redshift-binned upper luminosity limits are indicated as red lines. Their mean upper limit level is also indicated as the red upper limit on the histogram to the right.

241 clusters observed with *Chandra*. We cross-match between redMaPPer and the ACCEPT catalog within a 0′.5 aperture, resulting in 30 clusters. In Figure 3 we plot the Hα emission line luminosity as a function of central entropy, K_{20}, defined as the mean entropy inside 20 kpc. Clusters with no Hα detection (i.e., Flux_Ha_6562 = 0) are indicated as upper limits (arbitrary-level barred arrows; no error bars are given for these null measurements). As can be seen from the figure, the luminosities are anti-correlated with the central entropy, as previously reported. Specifically, below $K_{20} = 60$ keV cm^{-2} (pink dotted vertical line), the threshold we have used in M17 to separate CC from NCC clusters, all clusters have significantly higher luminosities, indicative of stronger cooling flows onto their BCG.

2.1.2. CC and NCC Sample Definitions

We now use the Hα luminosity information to create CC and NCC subsamples from the parent redMaPPer sample. First, we divide the sample evenly by the median luminosity value indicated by the dashed black line in both Figures 2 and 3. All clusters above this value are considered CC, while those below are considered NCC. However, selecting CCs based on Hα lines introduced a bias, because such features can be better determined at lower redshifts. This makes the redshift distribution of CCs skewed toward lower redshift with respect to that of NCCs. For this reason, we match the redshift distributions of the CC and NCC samples by downsampling both samples. This reduced the sample sizes further by ∼10% to about 3000 clusters in each. The redshift distributions of CC (blue) and NCC (red) subsamples after this procedure are presented in Figure 1. Their mean redshift is $\langle z \rangle = 0.25 \pm 0.06$.
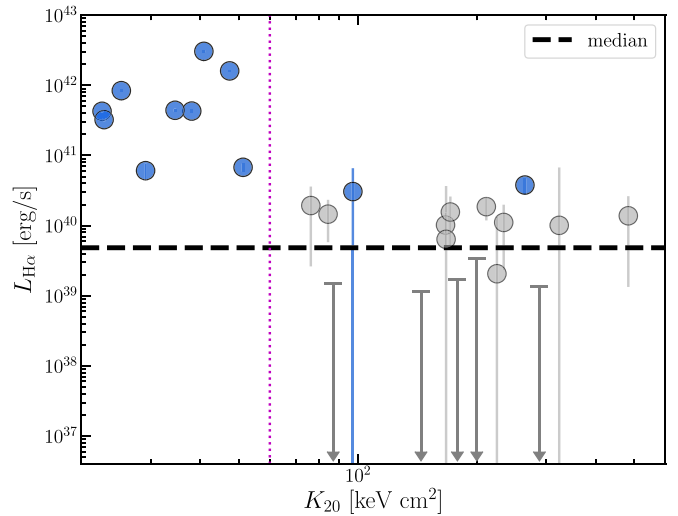

Figure 3. Hα luminosity as a function of central entropy inside 20 kpc, K_{20}, for each redMaPPer BCG having both spectra from SDSS and entropy measured from the ACCEPT (*Chandra*) database. Upper limits are drawn for BCGs with null Hα emission lines to mark the median luminosity level (dashed black line) we use to separate CC from NCC clusters, as in Figure 2. The entropy threshold of $K_{20} = 60$ keV cm^2 used in M17 to separate CC and NCC clusters is marked as a vertical dotted magenta line. Strong CC clusters are indicated as blue circles. Evidently, all clusters previously considered as CC by the entropy threshold are indeed strong CC clusters using the Hα definition.

As noted in the emissionLinePort documentation,[13] some fits to the spectra do not yield significant emission line flux measurements. Only those with amplitude-over-noise (AoN) >2 are considered significant emission line fluxes. We therefore select another more restrictive subset, "strong CC," of clusters with significant Hα flux (AoN_Ha_6562 > 2) totaling 485 clusters.[14] The strong CC sample is overlaid in Figure 2 and in Figure 3 (matched with ACCEPT) as blue circles. As can be seen from Figure 3, all nine clusters below our previous entropy-based definition ($K_{20} < 60$ keV cm^2) are considered strong CC based on the new Hα definition, and only two strong CC clusters are considered NCC based on their entropy. Raising the AoN threshold further to exclude those would cut the strong CC sample in half (∼280 clusters), too small for a statistically significant analysis.

We similarly select a restrictive "strong NCC" subset of clusters with null Hα line detection (i.e., Flux_Ha_6562 = 0), totaling 1778 clusters. To demonstrate the robustness of these null detections and their distinction from the CC population, we estimate an upper limit on the Hα luminosity using the continuum flux error at the Hα wavelength location. Since no errors were provided for the null Hα lines (Flux_Ha_6562 = 0), we take the continuum flux measured at Hα as an upper limit on the amplitude of the Hα line[15] and integrate the flux inside a Gaussian with a width of ∼100 km s^{-1} (∼2 Å). We plot these upper limits on the null detections as red lines in Figure 2 (binned in redshift for clarity). The mean level of these upper limits is given as a horizontal upper limit in the right histogram in Figure 2. The

---

13 https://www.sdss.org/dr12/spectro/galaxy_portsmouth/#kinematics
14 The strong CC and strong NCC redshift distributions are also matched, as was done for the CC/NCC samples.
15 We scale the continuum error up by a factor of $\sqrt{6800/100} \sim 8$, to account for the fact the continuum was estimated over the full spectral wavelength range, whereas the line would have been estimated over a narrower wavelength range, ∼100 Å.

Table 1
Galaxy and Cluster Samples Properties

Name	N	$\log\langle L_{\mathrm{H}\alpha}\rangle$ [ergs/s]	$M_{200\,\mathrm{m}}^{\lambda}$ $\times 10^{14}\,h^{-1}\,M_{\odot}$	$M_{200\,\mathrm{m}}^{\mathrm{lens}}$ $\times 10^{14}\,h^{-1}\,M_{\odot}$
LOWZ	239904			
redMaPPer	6687			
CC	3053	40.5	1.88 ± 0.03	$1.99_{-0.19}^{+0.21}$
NCC	3035	39.0	1.90 ± 0.03	$2.10_{-0.16}^{+0.18}$
Strong CC	485	41.0	1.83 ± 0.07	$1.99_{-0.40}^{+0.45}$
Strong NCC	1778	$\cdots$	1.91 ± 0.04	$2.11_{-0.21}^{+0.23}$

Note. Strong NCC are defined as clusters whose BCG has no Hα emission line detection; therefore no luminosity is indicated.

upper limits are also indicated in Figure 3. As can be seen, the upper limits on the null detections are well below the luminosity threshold above which clusters are considered CCs.

The redshift distributions of the strong CC and strong NCC are overlaid in Figure 1 as thick transparent blue and red lines, respectively. Their mean redshifts are the same as their parent CC/NCC samples. We summarize the basic properties of all the cluster subsamples in Table 1.

One limitation of the redMaPPer algorithm is that it a priori selects "red" galaxies as cluster members. For this reason, strong CC clusters with extreme star formation in their BCGs leading to bluer colors may be missing from this catalog. Rykoff et al. (2014) show examples of known CC clusters that are still detected, but their BCG is misidentified, leading to larger miscentering. In our above classification, such mis-identification may lead to assignment of a CC cluster as NCC. However, Rykoff et al. (2014) demonstrate that such catastrophic miscentering happens for roughly $\lesssim 5\%$ of all clusters. We therefore do not expect a large contamination of the NCC sample by CCs. However, as also indicated from the final sizes of our strong CC/NCC samples, this selection effect does diminish the number of strong CCs in the catalog.

2.1.3. Richness as a Mass Proxy

The bias of halos on galaxy cluster scales depends first and foremost on mass. Thus, it is important to ensure that the two cluster subsamples we compare have comparable mean mass before exploring any secondary dependencies on other properties. The redMaPPer catalog contains a richness measurement for each cluster, which can be considered as a mass proxy. Although richness is a very noisy mass proxy, our samples are large enough that the error on the mean mass of each sample is small. In the Appendix A, we will explore the level of uncertainty in the use of richness as a mass proxy by randomly subsampling from the redMaPPer sample. We present the richness distribution for the CC, NCC, strong CC, and strong NCC samples in Figure 4. The samples have consistent distributions, and their mean richness (and therefore, mass) are consistent within the errors. We list the mean mass based on the mass-richness relation from Simet et al. (2017) in Table 1.

We will further explore the mean masses of each cluster subsample using weak gravitational lensing in Section 4.1.
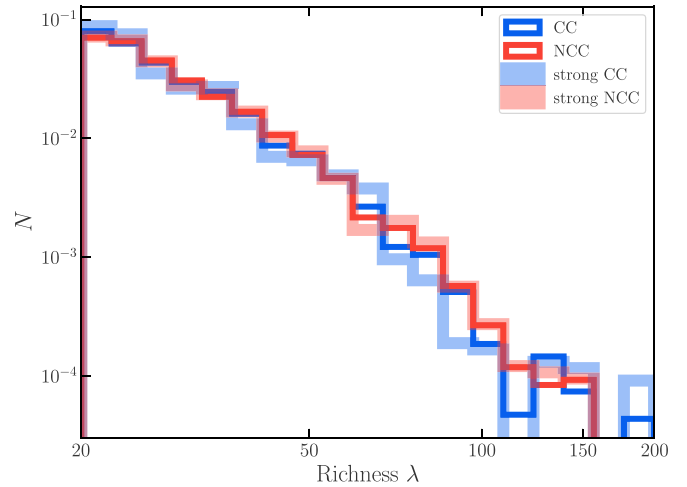

Figure 4. Normalized richness distribution of the different CC and NCC samples, as indicated in the legend.

2.2. LOWZ Galaxy Sample

We use the LOWZ spectroscopic-redshift galaxy catalog[16] (Reid et al. 2016), which is drawn from the Baryon Oscillation Spectroscopic Survey (BOSS; Dawson et al. 2013). BOSS is part of SDSS DR12 (Alam et al. 2015) and covers a total effective area of 8337 deg². The LOWZ sample is designed to extend the SDSS-I/II (York et al. 2000) Cut I luminous red galaxy sample (Eisenstein et al. 2001) to $z \approx 0.4$ and fainter luminosities, in order to increase the number density of luminous red galaxies by roughly a factor of 3. The LOWZ sample contains 463,044 galaxies with spectroscopic redshifts (Reid et al. 2016). A corresponding random catalog is also created by Reid et al. (2016) to mimic the LOWZ redshift distribution and describe the survey mask. It is constructed to be roughly ≈ 50 times the size of the LOWZ catalog. We limit both the galaxy catalog and the random catalog to the redshift range set by the redMaPPer catalog, $0.1 < z < 0.33$. The basic properties of the cluster and galaxy samples we use in the cross-correlation analysis are listed in Table 1.

3. Methods

In this section we detail the two independent methodologies we use for determining the level of assembly bias: clustering and WL.

3.1. Galaxy Clustering

Here we review the methodology developed in M17, cross-correlating a cluster sample with a larger galaxy sample in order to improve the statistical inference. The full details are given in M17, and so we only briefly summarize here.

The simple linear, deterministic galaxy bias relates between the galaxy overdensity, $\delta_{\mathrm{g}}(x)$, and the underlying matter overdensity, $\delta(x)$ (Kaiser 1984),

$$\delta_{\mathrm{g}}(x) = b_{\mathrm{g}}\delta(x), \qquad (1)$$

where overdensity is defined with respect to the mean density, $\delta(x) \equiv \rho(x)/\bar{\rho} - 1$. In practice, we make use of the two-point correlation function, $\xi(r) \equiv \langle \delta(x)\delta(x-r)\rangle$ (Peebles 1973, 1980). Under the above assumptions, the galaxy

---

16 https://data.sdss.org/sas/dr12/boss/lss/

bias relates the galaxy two-point auto-correlation to the underlying matter correlation function, such that,

$$\xi_g(r) = b_g^2 \xi_m(r). \tag{2}$$

Spectroscopic observations of galaxies typically allow us to measure the galaxy correlation function. In the linear, deterministic galaxy bias model, it is proportional to the correlation function of the underlying matter distribution, described by a constant factor.

One can alternatively cross-correlate different samples of galaxies, or galaxies and clusters as in our case. For the galaxy-cluster CCF, the above model yields

$$\xi_{g,cl}(r) = b_g b_{cl} \xi_m(r), \tag{3}$$

where b_g and b_{cl} denote the galaxy and the cluster bias, respectively. Since we correlate each of the two cluster samples (CC, NCC) with the same galaxy sample (LOWZ in our case), the ratio of these two cross-correlations simply traces the *relative* bias of NCC clusters with respect to CC clusters,

$$\ell^{(cross)}(r) \equiv b_{NCC}/b_{CC} = \frac{\xi_{g,NCC}(r)}{\xi_{g,CC}(r)}. \tag{4}$$

The galaxy bias term, b_g, automatically cancels out. Note that by using clustering alone (without assuming a halo model) one cannot constrain the individual cluster biases, b_{CC}, b_{NCC}, without assuming a cosmological model. We can instead constrain their ratio, the *relative* bias, defined as ℓ, and the superscript notation (cross) indicates the use of CCFs in the measurement.

Similarly, the ACF of clusters, $\xi_{cl}(r)$, would simply be

$$\xi_{cl}(r) = b_{cl}^2 \xi_m(r), \tag{5}$$

so that the relative bias can be derived from the CC and NCC autocorrelations as,

$$\ell^{(auto)}(r) = \sqrt{\frac{\xi_{NCC}(r)}{\xi_{CC}(r)}}. \tag{6}$$

The disadvantage of the ACF is that it is measured with a lower statistical precision compared with the CCF, because it requires the use of the smaller cluster sample.

3.2. Weak Lensing

WL induces a coherent tangential distortion to the shapes of background galaxies, proportional to the underlying halo excess surface mass density profile of the lensing cluster. The WL signal is related to the cluster-matter CCF and therefore allows us to both determine the halo total mass (to validate the CC/NCC samples have similar masses) and independently infer the linear bias parameter from the larger scales of the lensing profile.

The WL methodology as applied to SDSS has been extensively reviewed in the literature (e.g., Mandelbaum et al. 2005, 2013; Simet et al. 2017; Murata et al. 2018), so we only briefly summarize it here. We estimate the mean projected cluster mass density excess profile $\Delta\Sigma(r)$ by stacking the shear (as measured from the ellipticities) of source galaxies s over multiple clusters l that lie within a given cluster-centric radial annulus r,

$$\Delta\Sigma(r) = B(r)\frac{1}{2\mathcal{R}}\frac{\sum_{l,s} w_{ls} e_{t,ls} \Sigma_{cr,ls}}{\sum_{l,s} w_{ls}}, \tag{7}$$

where the double summation is over all clusters and over all sources associated with each cluster (i.e., lens-source pairs). The critical surface mass density is defined as $\Sigma_{cr} = \frac{c^2}{4\pi G}\frac{D_A(z_s)}{D_A(z_l)D_A(z_l,z_s)(1+z_l)^2}$, where G is the gravitational constant, c is the speed of light, z_l and z_s are the lens and source redshifts, respectively, and $D_A(z_l)$, $D_A(z_s)$, and $D_A(z_l, z_s)$ are the angular diameter distances to the lens, the source, and the lens to source, respectively. The extra factor of $(1 + z_l)^2$ comes from our use of comoving coordinates (Bartelmann & Schneider 2001). The photometric redshifts of source galaxies were estimated with ZEBRA, and a photometric redshift bias correction was applied (Nakajima et al. 2012). The minimum variance estimator requires the weights to be $w_{ls} = \frac{1}{\Sigma_{cr,ls}^2}\frac{1}{\sigma_{e,ls}^2 + e_{rms}^2}$, where σ_e is the shape measurement uncertainty due to pixel noise and $e_{rms} = 0.365$ is the intrinsic shape noise. The "shear responsivity" factor, $2\mathcal{R}$, represents the response of the ellipticity, e, to a small shear (Kaiser 1995; Bernstein & Jarvis 2002). The factor $B(r)$, corresponds to the boost factor needed to correct for the dilution effect, which arises from contamination by unlensed cluster galaxies having imperfect photometric redshift estimates. The boost is estimated by comparing the weighted number density of source-lens pairs to that around random points, $B(r) = \frac{N_r \sum_{ls} w_{ls}}{N_l \sum_{rs} w_{rs}}$.

Following Miyatake et al. (2016), we fit each lensing profile with a five-parameter model,

$$\Delta\Sigma(r; M_{200\,m}, c_{200\,m}, q_{cen}, \alpha_{off}, b)$$
$$= q_{cen}\Delta\Sigma^{NFW}(r; M_{200\,m}, c_{200\,m})$$
$$+ (1 - q_{cen})\Delta\Sigma^{NFW,off}(r; M_{200\,m}, c_{200\,m}, \alpha_{off})$$
$$+ \Delta\Sigma^{2-halo}(r; b). \tag{8}$$

The first term arises from the halo mass profile for a fraction q_{cen} of clusters whose BCGs as identified by redMaPPer represent the true cluster centers, while the second term describes the profile of the off-centered clusters. We assume that the offsets follow a Gaussian distribution in three dimensions, with $u_{off} \propto \exp[-r^2/(2\alpha_{off}^2 r_{200\,m}^2)]$, where α_{off} describes the ratio of the off-centering radius to $r_{200\,m}$, the radius at which the enclosed mass density is 200 times the mean density of the universe. For both components we adopt the smoothly truncated Navarro–Frenk–White (NFW; Navarro et al. 1996) model (Oguri & Hamana 2011). The final term models the contribution from the surrounding LSS, that is, the two-halo term. We employ the model given as $\Delta\Sigma^{2-halo}(r; b) = b\int k\,dk/(2\pi)\bar{\rho}_m P_m^L(k; z_{cl})J_2(kr)$, where $\bar{\rho}_m$ is the mean mass density today, b is the linear bias parameter, and $P_m^L(k; z_{cl})$ is the linear mass power spectrum at the averaged cluster redshift $z_{cl} = 0.25$, for the ΛCDM model. We treat the mass, $M_{200\,m}$, and galaxy bias, b, independently because we do not want the mass estimate to be influenced by the presence of assembly bias. If we were to assume a bias–mass relation (e.g.,
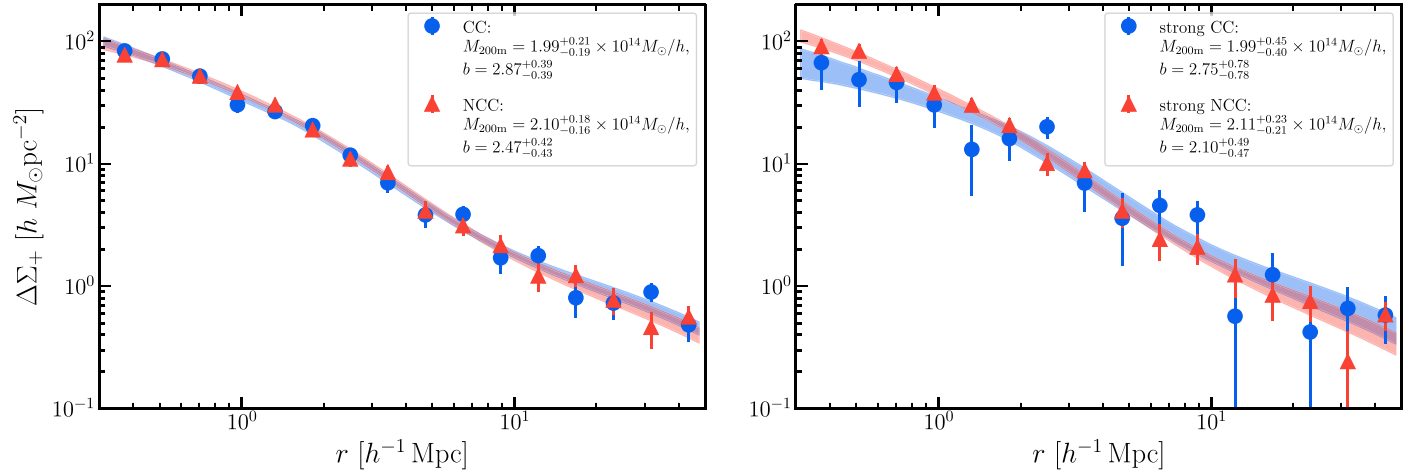
Figure 5. Stacked cluster WL excess surface mass density profiles for the CC and NCC samples (left) and the strong CC/NCC samples (right). Mean masses and halo bias values derived from model fitting the WL profiles are given next to each set. The NCC mean mass is about 1σ above the CC mass (see Table 1), whereas the CC galaxy bias is about 1σ above the NCC galaxy bias (and similarly for the strong CC/strong NCC samples).

Tinker et al. 2010), then the presence of assembly bias in our measurement would bias our mass estimate.

We can then directly probe the relative bias from the individual bias parameters fitted to the lensing profile, defined as

$$\ell^{2h} \equiv \frac{b_{\rm NCC}}{b_{\rm CC}}. \qquad (9)$$

As a baseline expectation, we can use the halo bias model of Tinker et al. (2010), calibrated from numerical simulations, in order to estimate the *expected* halo bias level for each sample based on the derived mean WL mass. Under the zeroth order assumption of no assembly bias, we can then define the expected relative bias as,

$$\ell^0 \equiv \frac{b(M_{\rm NCC})}{b(M_{\rm CC})}. \qquad (10)$$

Any deviation from this value should therefore give an estimate of the level of assembly bias. Specifically, we define f as the ratio of the measured bias from each methodology defined above (e.g., $\ell^{\rm (cross)}$, $\ell^{\rm (auto)}$, ℓ^{2h}) to the expected mass-only bias, ℓ^0, such that our model for the measured bias is

$$\ell = f\ell^0. \qquad (11)$$

Confirmation of assembly bias requires $f \neq 1$. We will therefore obtain the marginalized posterior distribution of f from fitting the above model to each measured relative bias. We perform the fitting with the public code EMCEE (Foreman-Mackey et al. 2013).

4. Results

In this section we present the WL and clustering analyses of the CC and NCC cluster samples defined above and the mean relative bias we derive for each methodology.

4.1. Weak Lensing

Here we make use of lensing data to first determine the mean masses of the CC and NCC cluster samples and test whether they are indeed comparable as indicated by the mass-richness scaling relation. Subsequently, cluster WL profiles will be used

to determine the level of expected mass bias and the level of measured bias.

We use the SDSS/DR8 shape catalog (Reyes et al. 2012; Mandelbaum et al. 2013) measured with the re-Gaussianization technique (Hirata & Seljak 2003). The systematic uncertainties on shape measurements have been thoroughly investigated in Mandelbaum et al. (2005). We measure the stacked WL excess surface mass density profile, $\Delta\Sigma(r)$ (Equation (7)), in 16 logarithmically spaced radial bins in the range 0.3–50 h^{-1} Mpc. We present the resulting profiles in Figure 5 for both the CC/NCC (left, circles and triangles, respectively) and the strong CC/NCC (right) samples. The covariance is derived using the jackknife method, dividing the sample into 83 equal area bins. The figure demonstrates that the two subsamples have very similar mass profiles.

We fit for both the one- and two-halo terms simultaneously, setting flat priors on the mass, $M_{200\,m}$, concentration, $c_{200\,m}$, and halo bias b. We set restrictive Gaussian priors on the miscentering parameters, around the nominal values presented in Simet et al. (2017). We do this because the profiles are not well constrained at the center, $r < 300$ kpc, and miscentering is highly degenerate with the concentration parameter. For the same reason, we do not fit for a central stellar mass contribution from the BCG. The fitted masses are listed for each cluster sample in Table 1. We find overall consistent masses for the CC/NCC samples, $M_{\rm CC} = 1.99^{+0.21}_{-0.19} \times 10^{14}\ h^{-1}\ M_\odot$ and $M_{\rm NCC} = 2.10^{+0.18}_{-0.16} \times 10^{14}\ h^{-1}\ M_\odot$. The strong CC/NCC samples also show similarly consistent masses, $M_{\rm stCC} = 1.99^{+0.45}_{-0.40} \times 10^{14}\ h^{-1}\ M_\odot$ and $M_{\rm stNCC} = 2.11^{+0.23}_{-0.21} \times 10^{14}\ h^{-1}\ M_\odot$. For both cases, mean masses are consistent within 1σ.

As presented in Section 3.2, we can calculate the expected mass-only bias (Equation (10)). Using the Tinker et al. (2010) halo bias model provided in the python COLOSSUS tool kit (Diemer 2018), we translate each lensing mass predicted by the Markov chain Monte Carlo process to galaxy bias. We then derive the relative bias by dividing each of NCC bias values with each of the CC bias values. The expected bias ratio of CC and NCC clusters is $\ell^0 = 1.05^{+0.07}_{-0.06}$. For the strong CC and strong NCC samples, the expected relative bias is $\ell^0 = 1.05^{+0.13}_{-0.11}$. Therefore, based on the masses, the LSS around NCC is not expected to be significantly more clustered

Table 2
Results of the Bias Analysis from Different Methodologies

Method	CC/NCC		Strong CC/NCC	
	ℓ	f	ℓ	f
Lensing				
1-halo (expected)	$1.05^{+0.07}_{-0.06}$	1	$1.05^{+0.13}_{-0.11}$	1
2-halo	$0.86^{+0.20}_{-0.20}$	$0.83^{+0.20}_{-0.20}$	$0.89^{+0.67}_{-0.54}$	$0.86^{+0.66}_{-0.52}$
Clustering				
$\xi_{g,cl}$	$1.01^{+0.03}_{-0.03}$	$0.97^{+0.07}_{-0.06}$	$0.98^{+0.06}_{-0.06}$	$0.94^{+0.13}_{-0.11}$
$\xi_{g,cl}$, projected	$0.97^{+0.06}_{-0.06}$	$0.93^{+0.08}_{-0.08}$	$0.82^{+0.10}_{-0.10}$	$0.79^{+0.13}_{-0.12}$
ξ_{cl}	$1.02^{+0.06}_{-0.06}$	$0.98^{+0.08}_{-0.08}$	$0.97^{+0.22}_{-0.22}$	$0.93^{+0.25}_{-0.23}$

Note. The expression $\ell = b_{NCC}/b_{CC}$ measures the level of relative bias between the NCC and CC clusters; $f = \ell/\ell^0$ measures the level of assembly bias. Median and 68% confidence bounds are quoted.

than around CC clusters ($\lesssim 5\%$). These results are summarized in the first row of Table 2.

In comparison, the linear biases directly estimated from the two-halo fit show a ratio that is statistically consistent with that expected from the lensing masses, though the central value is about 1σ below. In the case of CC/NCC, we measure $b_{CC} = 2.87 \pm 0.39$ and $b_{NCC} = 2.47^{+0.42}_{-0.43}$. As defined in Equation (9), this translates to a relative bias of $\ell^{2h} = 0.86 \pm 0.20$. For the strong CC/NCC samples, we find $b_{stCC} = 2.75 \pm 0.78$ and $b_{stNCC} = 2.10^{+0.49}_{-0.47}$, that is, a relative bias of $\ell^{2h} = 0.89^{+0.67}_{-0.54}$. The two-halo bias results are summarized in the second row of Table 2. We will quantify the significance and interpretation of these different results in Section 5.1, together with the two-point clustering results presented next.

4.2. Clustering

Here we measure the relative bias from the clustering profiles on large scales using the two-point correlation functions as defined in Section 3. We make use of the public code CORRFUNC (Sinha & Garrison 2017), which relies on the Landy & Szalay (1993) estimator, to calculate all the two-point redshift-space correlation functions. We first compute the CCF of each cluster subsample (CC, NCC, strong CC, and strong NCC) with the LOWZ galaxies. In order to avoid redshift-space distortions (RSDs) that affect galaxies infalling into halos, we need to compute the CCF outside the cluster one-halo regime. We evaluate this scale by computing the velocity dispersion of each cluster subsample from the peculiar velocities of LOWZ galaxies inside $1.5\ h^{-1}$ Mpc of a nearby cluster halo. The CC and NCC samples show $\sigma_v \simeq 700$ km s^{-1}, corresponding roughly to a virial radius of $1\ h^{-1}$ Mpc. We furthermore compute the two-dimensional CCF as a function of projected (r_p) and line-of-sight (π) distance, $\xi(r_p, \pi)$. Finger-of-god effects are evident up to scales $\lesssim 10\ h^{-1}$ Mpc. We therefore choose to compute the CCF (Equation (3)) in six logarithmic bins in the range 10–80 h^{-1} Mpc. Throughout, the full covariance matrix is derived using the jackknife method for each of the correlation functions and the bias profiles, by dividing the SDSS/redMaPPer area into 192 equal area regions. The results are presented in the top panels of Figure 6. The top panel of the left plot shows the CCFs, $\xi_{g,cl}(r)$, of the CC (blue) and NCC (red) clusters, and the

bottom panel shows the bias, $\ell^{(cross)}(r)$ (black), derived from the ratio of the two CCFs (Equation (4)). The right panel shows the same for the strong CC and strong NCC cluster subsamples. To estimate the mean bias level we fit $\ell(r)$ with a constant model taking into account the covariance between scales. The median relative bias, $\ell^{(cross)}$, and its uncertainty are summarized in Table 2. Apparently, there is no significant difference between the clustering around CC versus NCC, $\ell^{(cross)} = 1.01 \pm 0.03$. The bias for strong CC/NCC is also nonsignificant, $\ell^{(cross)} = 0.98 \pm 0.06$.

Another common methodology is to calculate the ACF of the clusters themselves, $\xi_{cl}(r)$, given by Equation (5), where the relative bias equals the square root of the ratio of the ACFs (Equation (6)). Naturally, this methodology yields larger errors but may serve as a semi-independent check of the bias, because the LOWZ galaxy sample is not included here. We present the results for the CC/NCC and strong CC/NCC samples in the bottom plots of Figure 6. The ACF also shows a bias fully consistent with the expected level, $\ell^{(auto)} = 1.02 \pm 0.06$ for the CC/NCC and $\ell^{(auto)} = 0.97 \pm 0.22$ for the strong CC/NCC. The results are summarized in the last row of Table 2. We will compare the clustering results with those derived from lensing and interpret them in the context of assembly bias in Section 5.1.

Lastly, to validate that the CCF are not affected by RSD effects, we also compute the projected 2D CCF, $w_p(r_p)$, integrated along the line of sight to $\pi = 100\ h^{-1}$ Mpc. Such integration removes any issues due to RSD. The results, shown as dashed lines in Figure 7, are consistent with those derived from the CCF, $\xi_{g,cl}(r)$.

5. Discussion

5.1. Significance of Assembly Bias

We now explore the level of assembly bias derived from each methodology by comparing it with the expected mass-only bias level, ℓ^0, derived from the fitted lensing masses. To visualize these, in Figure 8 we plot the fiducial bias profile measured from the ratio of CCFs, $\ell^{(cross)}$ (black; same as solid black line in Figure 6). We overlay the lensing-measured relative bias using the fitted bias parameters, ℓ^{2h} (hatched, 68% confidence region) and finally the expected mass-only bias derived by assuming a Tinker et al. (2010) halo bias model with the WL mean masses as input, ℓ^0 (pink, 68% confidence region). It appears that $\ell^{(cross)}$ agrees well with the level derived from the lensing two-halo term, ℓ^{2h}, although the constraints on the latter are poor ($\sim 20\%$–60% confidence level). On the other hand, both measured biases, $\ell^{(cross)}$ and ℓ^{2h}, are about 1σ below the expected level, ℓ^0.

To better quantify whether the measured bias significantly differs from the expected mass-only bias ℓ^0, we fit each measured data set (ℓ^{2h}, $\ell^{(cross)}(r)$, projected $\ell^{(cross)}(r_p)$ and $\ell^{(auto)}(r)$) with the model described in Equation (11). For all the clustering results, which were determined as a function of scale, we take into account the full covariance matrix in our likelihood function. Since our parameter of interest is f, we set a flat (uninformative) prior on f. We set a tight lognormal prior on ℓ^0 dictated by the median and standard deviation of $\log(\ell^0)$ and then marginalize over it. The posterior values for f are given in Table 2 next to each measured ℓ.

As can be seen, all values of f are consistent with the null hypothesis, $f = 1$, up to 1–2σ. The projected $\ell^{(cross)}$ measured
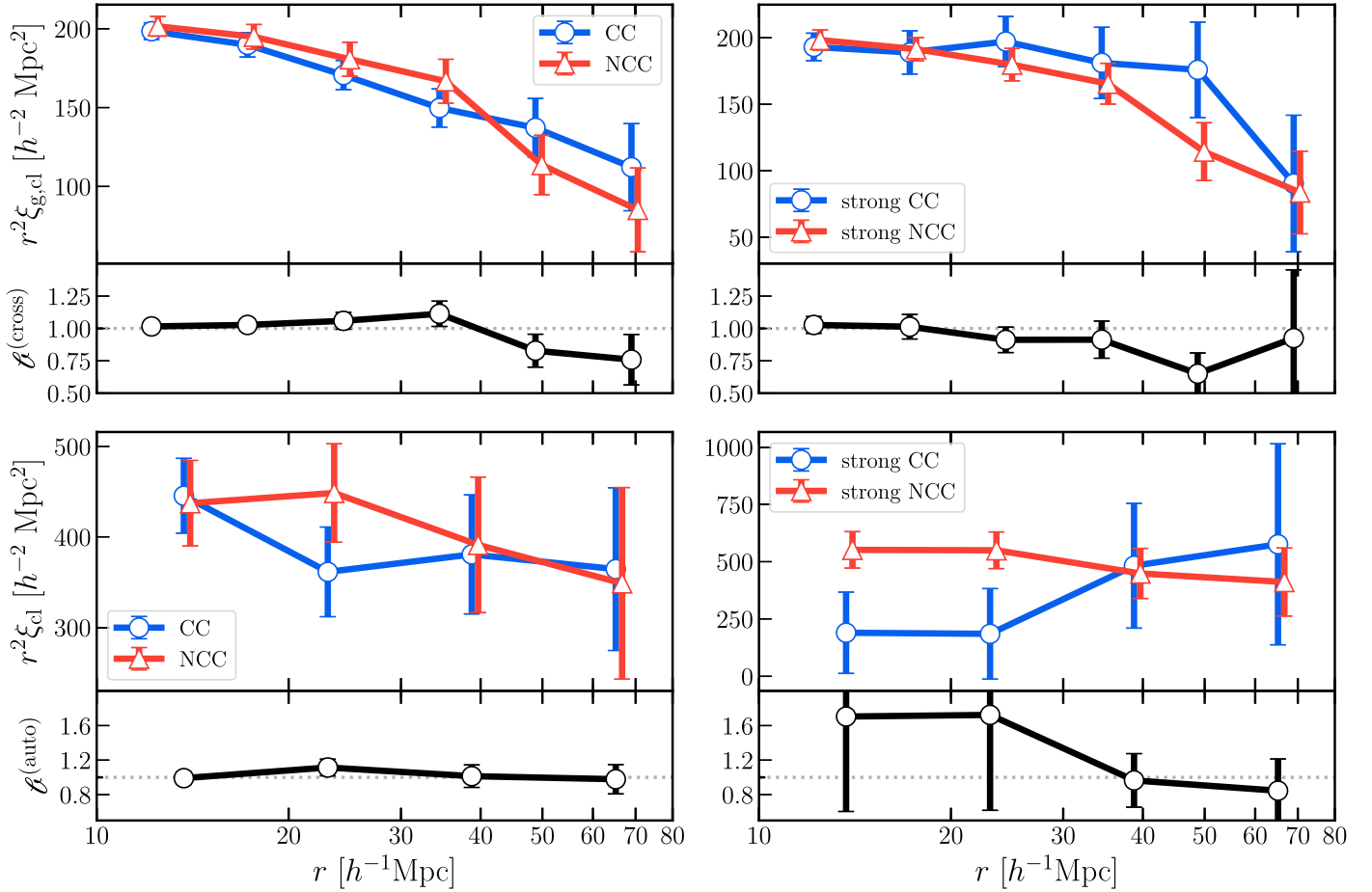
Figure 6. Each top panel in the plots shows the two-point correlation functions for the CC (blue) and NCC (red), while the bottom panels show the relative bias (black) derived from the ratio of the CC/NCC correlation functions above it, as a function of comoving separation, r. Left plots show the results for the median-divided CC/NCC samples, whereas right plots show the strong CC/NCC samples (see Table 1 for definitions). Top and bottom plots use different clustering methodologies. Top: using the CCFs between galaxies and clusters, $\xi_{g,cl}(r)$. Bottom: using the ACFs of the cluster samples, $\xi_{cl}(r)$. Overall, the results are consistent between the different methodologies. The CCF methodology, however, yields tighter constraints than the ACF due to the larger galaxy sample employed.

for the strong CC/NCC samples shows the highest offset, $f = 0.79 \pm 0.12$ but is still below the 2σ level. We therefore conclude, based on the best-constrained CCF measurement of assembly bias, f, that there is no indication of different assembly histories for CC and NCC clusters to within 6% uncertainty.

5.2. Comparison with Simulations

In simulations, assembly bias on cluster scales has been shown to exist in practically all definitions of halo age (Chue et al. 2018), although some proxies appear to be noisier than others (Mao et al. 2018). Recently, combining several N-body simulations covering a wider mass range up to $10^{14.5}h^{-1}\,M_\odot$, Sato-Polito et al. (2019) find different secondary indicators of assembly histories yield somewhat different results. For example, if separating halos by their age, no assembly bias is detected above $\times 10^{14}\,h^{-1}\,M_\odot$. On the other hand, if separating halos by concentration or spin, at the high-mass end, the difference between the upper and lower quartiles can reach up to a factor of 2.

There is no equivalent in cosmological simulations for the physical distinction we are studying, that is, the cooling phase of the cluster core gas. This is because baryonic effects, especially considering the large range in scales involved, are currently hard to include (although see Rasia et al. 2015;

Barnes et al. 2018). Therefore, any statements about the levels found in simulations are not necessarily applicable to our study. Nonetheless, we may consider the above range of bias values found in simulations as a guideline to the degree of assembly bias expected in general. With that in mind, it is safe to conclude we find no significant level of assembly bias in our samples.

5.3. Alternative Scenarios

Given this measurement alone, we may not identify the specific formation model. Whether cores are created early on and left undisturbed, or whether later periodic CC formation and disruption are at play, we find those to be decoupled from the external environment on large scales. One may argue this is not surprising because the cores are embedded in self-similar envelopes (McDonald et al. 2017). It may be that even though their large-scale modes appear the same, small-scale fluctuations result in different initial conditions at the halo regime ($r \lesssim 1$ Mpc); for example, NCC may be the result of a lower amplitude fluctuation with a higher level of substructure. If, on the other hand, no small-scale differences are found, one could imagine a scenario in which the formation of CC or NCC is set by short-term random local ($r < 200$ kpc) processes such as infall of small groups or AGN feedback (Gaspari et al. 2014), causing episodic transitions between CC and NCC (Rossetti &
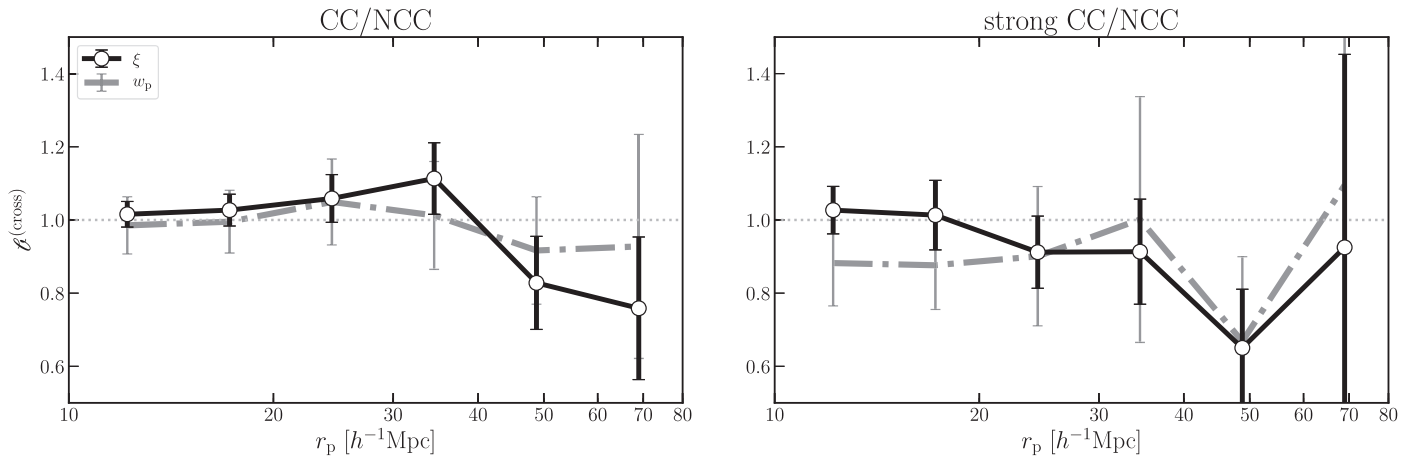
Figure 7. Relative bias from cross-correlation as a function of separation, but calculated using the *projected* CCF, $w_{\rm p}(r_{\rm p})$ (gray dashed–dotted line). The signal is consistent with that derived from the 3D CCF (black, same as the black solid lines in the top plots of Figure 6).

Molendi 2010). However, this scenario is less likely due to the long cooling times of most NCC clusters. It would thus be interesting to compare the small-scale clustering of CC and NCC clusters at low and high redshift. As apparent from our analysis, WL alone is not sensitive enough to distinguish between cluster profiles at such small scales. On the other hand, a combination of strong and WL at the one-halo regime should provide more robust constraints on the cluster profile shape. Such investigations are the subject of a future study.

6. Summary and Conclusions

In this paper we tested the level of assembly bias between different cluster samples, separated by a physically motivated criteria: the level of cooling in their cores. We differentiate between CC and NCC clusters solely based on the BCG Hα luminosity as a cooling indicator. We draw samples of thousands of CC and NCC clusters from the SDSS/DR8 redMaPPer catalog to achieve a statistically significant measurement of the weak assembly bias effect. We performed a WL analysis measuring the cluster density profiles to investigate their mean mass and two-halo linear bias properties. Furthermore, we applied a complementary and novel methodology, cross-correlating the cluster samples with an even larger sample of hundreds of thousands of galaxies from the LOWZ sample, to gain better statistical precision on the bias. This method provides information on the large-scale environments of clusters that have apparently different characteristics, which in turn provide insight into their formation history.

From WL we found the CC and NCC samples to have comparable mean masses, $M_{\rm 200m} \approx 2 \times 10^{14}\, h^{-1}\, M_\odot$. From the mean WL masses, we quantified the expected level of mass-only bias to be $\ell^0 = 1.05^{+0.07}_{-0.06}$ for the CC/NCC samples and $\ell^0 = 1.05^{+0.13}_{-0.11}$ for the strong CC/NCC samples. We then quantified the departure from the null hypothesis with the assembly bias fraction, f, and fitted the measured bias to constrain this parameter. From the lensing two-halo measured bias, $\ell^{\rm 2h}$, we found no indication of assembly bias, with $f = 0.83 \pm 0.20$ for CC/NCC and $f = 0.86^{+0.66}_{-0.52}$ for the strong CC/NCC. Since the size of the error is approximately at or greater than the expected level of the effect, $\sim$20%–70%, for the current sample size lensing alone lacks statistical constraining power to probe assembly bias.

From the more sensitive CCF methodology, we fit $\ell^{\rm (cross)}$ and found $f = 0.97^{+0.07}_{-0.06}$ for the CC/NCC samples and $f = 0.94^{+0.13}_{-0.11}$ for the strong CC/NCC samples. We also applied the more traditional ACF methodology using the clusters alone and found $f = 0.98 \pm 0.08$ for CC/NCC and $f = 0.93^{+0.25}_{-0.23}$ for the strong CC/NCC, although this methodology is statistically weaker, with constraining power similar to that of the lensing methodology. Therefore, within $\sim$1σ, both subsets using both methodologies agree with no assembly bias.

It is important to note that although we have expanded our analysis to make use of thousands of clusters compared with dozens in M17, the redMaPPer sample is inherently biased against heavily star-forming cluster cores (Rykoff et al. 2016). Indeed, our strong CC sample is limited to $\sim$500 clusters only. A future study would benefit from a less biased sample, for example, not relying on a red-sequence finder (e.g., Soares-Santos et al. 2011; Wen et al. 2012) or one that makes use of future all-sky redshift surveys (e.g., SPHEREx; Doré et al. 2016).

We conclude, based on the results presented in this analysis, that any observed differences between CC and NCC clusters are not inherited from different large-scale environments. In turn, the assignment of the cluster cooling phase may result from different small-scale clustering. Combined with the reported mild evolution in CC properties, one possible solution is that the local gas properties in the protocluster core determine the subsequent creation of an AGN feedback loop. Alternatively, local ($r < 200$ kpc) merger activity could create and destroy CC periodically but in a way that mimics constant mean population properties over time.

While our study cannot confirm either proposed picture, studying clusters at the onset of formation, which appears to be as high as $z \sim 2$, can shed direct light on the process of core formation. We are only now at a stage where the evolution of clusters can be studied statistically with large ensembles, both in observations (McDonald et al. 2017, 2018) and in cosmological simulations (Rasia et al. 2015; Barnes et al. 2018). Such large-scale simulations are in the infancy of incorporating complex AGN feedback and feeding physics via subgrid models and require better physically motivated (rather than fine-tuned) schemes in order to achieve robustly predictive results for the CC-NCC formation (e.g., Gaspari & Sądowski 2017). LSST and *WFIRST* will revolutionize our
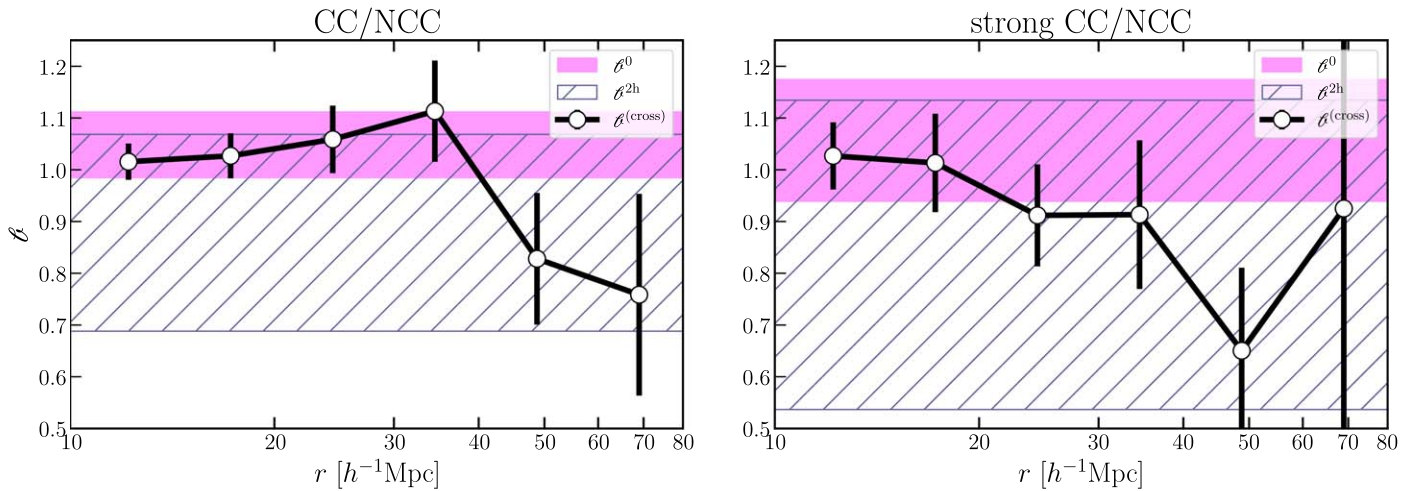
Figure 8. Comparison of the relative bias measured with cross-correlation, $\ell^{(\text{cross})}(r)$ (black points, same as in top panels of Figure 6) and with lensing, $\ell^{2\text{h}}$ (68% confidence region; hatched). These two are compared with the level of expected mass-only relative bias ℓ^0 (68% confidence region; pink), calculated using the Tinker et al. (2010) halo bias model with the WL-derived masses as input. The two measurements are consistent within $\lesssim 1\sigma$ with the expected mass-only bias level, for both the CC/NCC and strong CC/NCC samples, that is, showing no evidence for assembly bias between CC and NCC.

understanding of cluster formation and evolution, as they will enable us to study the galaxy populations in $z \lesssim 2$ clusters in the thousands instead of the current dozens. CMB-S4 will both detect clusters up to $z \sim 2$ through the redshift-independent SZ effect and inform on the gas properties at the epoch of cluster formation. Our most pressing challenge is matching those promising optical/IR surveys with the complementary high-resolution spectral and X-ray surveys of cluster cores (e.g., *Athena*; Ettori et al. 2013) that will facilitate better understanding of the initial buildup and the precise impact of baryonic physics on cluster formation.

Appendix A
Null Test

We perform a null test to validate that our CCF methodology yields no bias ($\ell = 1$) when selecting cluster subsamples randomly. From the parent redMaPPer sample, we select 100 random subsamples each of the same size as our CC/NCC samples ($N = 3000$). We perform the same CCF analysis as described in Section 4.2, cross-correlating each random subsample with the LOWZ catalog. We divide each of the CCFs of the first 50 subsamples ("rand1") with each of the CCFs of the last 50 subsamples ("rand2") to get 50^2 relative bias realizations. The results are presented in Figure 9 (left). Errors represent the scatter from the random sampling. These errors also take into account both statistical noise and systematics due to the assumption that equal richness distributions represent equal masses. These errors are comparable to the jackknife errors that we use as our fiducial errors.

Appendix B
Mass Bias Test

In this section we test that our CCF methodology retrieves the expected mass bias. For this test, we use the Marenostrum Institut de Ciènćies de l'Espai (MICE) Grand Challenge (MICE-GC) version 1 simulations[17] (Carretero et al. 2015; Crocce et al. 2015; Fosalba et al. 2015a, 2015b; Hoffmann et al. 2015). For each mock galaxy, observational properties such as R.A., decl., redshift (including peculiar velocities), and g, r, i, z magnitudes are provided. The halo mass is also known. We define clusters as having $M_\text{h} > 10^{13}\,M_\odot$. We randomly select 20 bootstrap realizations of cluster samples each of size $N = 3000$, in each of the six mass bins. We cross-correlate each cluster sample with a mock galaxy sample (which we select to mimic the LOWZ sample in terms of color and
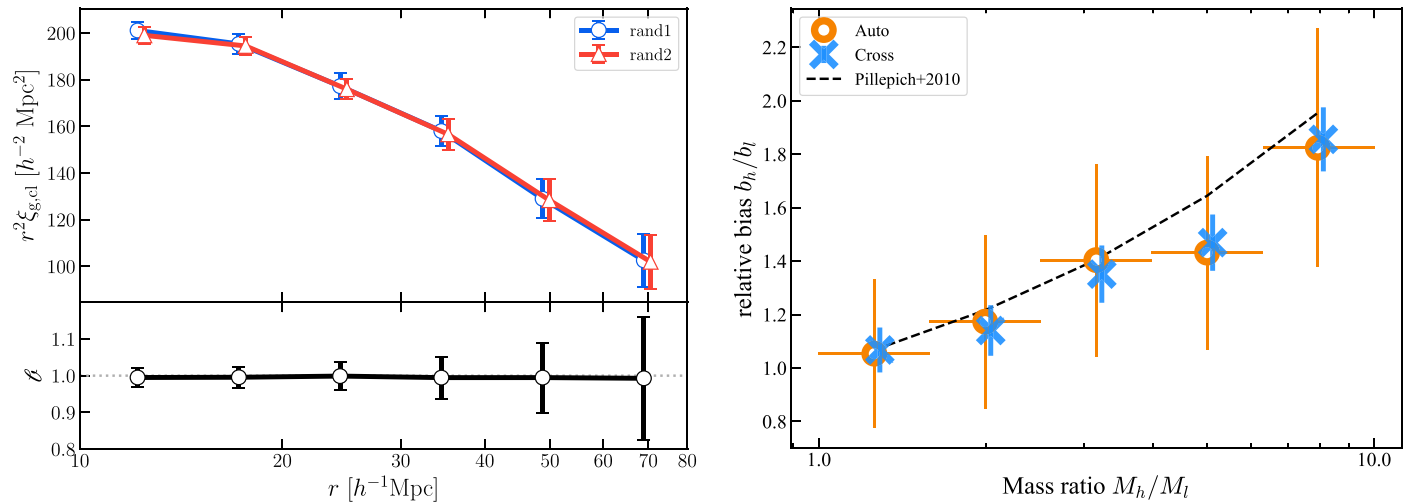
---

[17] https://cosmohub.pic.es

Figure 9. Left: results from the null test. We randomly select subsamples from the parent redMaPPer catalog and calculate the CCFs and relative bias, clearly validating the null hypothesis: $b = 1$ between two random subsamples. Right: results from the mass bias test. The theoretical relation between relative halo mass bias and the mass ratio is given by the black dashed line, based on Pillepich et al. (2010) simulations. Orange circles and blue crosses show the relative bias in each mass ratio bin measured from simulated MICE clusters and galaxies using the ACF and CCF, respectively. The ACF and CCF methodologies give consistent results, and both are consistent with the expected level.

redshift distribution) over the entire radial range ($10–80\,h^{-1}$ Mpc, as for our data) and divide each of the CCFs of the five highest mass bins with the CCF of the lowest mass bin. This gives us a test of our CCF methodology: the ratio should give the relative mass bias, $\ell^{(\mathrm{cross})}$. Since we have 20 mock cluster catalogs in each mass bin, we have overall 400 realizations of the relative bias in each mass ratio bin. We take the scatter as the error on the relative bias. We follow the same exercise for the ACF methodology, measuring $\ell^{(\mathrm{auto})}$. We plot the expected (black; using the Pillepich et al. 2010 model) and the derived $\ell^{(\mathrm{cross})}$ (blue crosses) and $\ell^{(\mathrm{auto})}$ (orange circles) averaged over all scales as a function of mass ratio in Figure 9 (right). As can be seen, the two methodologies are completely consistent with each other. As expected, the CCF methodology yields much smaller uncertainties than the ACF. The CCF-derived $\ell^{(\mathrm{cross})}$ is slightly below the expected values found by Pillepich et al. (2010), but only at high mass ratios (our study is at a mass ratio of $\lesssim 1.2$, as determined in Section 4.1). We also note that different approaches adopted by different simulation sets may cause this small effect.

ORCID iDs

Elinor Medezinski ⓘ https://orcid.org/0000-0001-7007-2358
Surhud More ⓘ https://orcid.org/0000-0002-2986-2371
Massimo Gaspari ⓘ https://orcid.org/0000-0003-2754-9258

References

Alam, S., Albareti, F. D., Allende Prieto, C., et al. 2015, ApJS, 219, 12
Barnes, D. J., Vogelsberger, M., Kannan, R., et al. 2018, MNRAS, 481, 1809
Bartelmann, M., & Schneider, P. 2001, PhR, 340, 291
Bernstein, G. M., & Jarvis, M. 2002, AJ, 123, 583
Busch, P., & White, S. D. M. 2017, MNRAS, 470, 4767
Carretero, J., Castander, F. J., Gaztañaga, E., Crocce, M., & Fosalba, P. 2015, MNRAS, 447, 646
Cavagnolo, K. W., Donahue, M., Voit, G. M., & Sun, M. 2008, ApJ, 682, 821
Cavagnolo, K. W., Donahue, M., Voit, G. M., & Sun, M. 2009, ApJS, 182, 12
Chue, C. Y. R., Dalal, N., & White, M. 2018, JCAP, 10, 012
Correa, C. A., Wyithe, J. S. B., Schaye, J., & Duffy, A. R. 2015, MNRAS, 452, 1217
Crocce, M., Castander, F. J., Gaztañaga, E., Fosalba, P., & Carretero, J. 2015, MNRAS, 453, 1513
Croton, D. J., Gao, L., & White, S. D. M. 2007, MNRAS, 374, 1303
Dawson, K. S., Schlegel, D. J., Ahn, C. P., et al. 2013, AJ, 145, 10
Diemer, B. 2018, ApJS, 239, 35
Donahue, M., Mack, J., Voit, G. M., et al. 2000, ApJ, 545, 670
Doré, O., Werner, M. W., Ashby, M., et al. 2016, arXiv:1606.07039
Edge, A. C. 2001, MNRAS, 328, 762
Eisenstein, D. J., Annis, J., Gunn, J. E., et al. 2001, AJ, 122, 2267
Eisenstein, D. J., Weinberg, D. H., Agol, E., et al. 2011, AJ, 142, 72
Ettori, S., Pratt, G. W., de Plaa, J., et al. 2013, arXiv:1306.2322
Fabian, A. C. 1994, ARA&A, 32, 277
Fabian, A. C. 2012, ARA&A, 50, 455
Faltenbacher, A., & White, S. D. M. 2010, ApJ, 708, 469
Foreman-Mackey, D., Hogg, D. W., Lang, D., & Goodman, J. 2013, PASP, 125, 306
Fosalba, P., Crocce, M., Gaztañaga, E., & Castander, F. J. 2015a, MNRAS, 448, 2987
Fosalba, P., Gaztañaga, E., Castander, F. J., & Crocce, M. 2015b, MNRAS, 447, 1319
Gao, L., Springel, V., & White, S. D. M. 2005, MNRAS, 363, L66
Gao, L., & White, S. D. M. 2007, MNRAS, 377, L5
Gaspari, M. 2015, MNRAS, 451, L60
Gaspari, M., Churazov, E., Nagai, D., Lau, E. T., & Zhuravleva, I. 2014, A&A, 569, A67
Gaspari, M., McDonald, M., Hamer, S. L., et al. 2018, ApJ, 854, 167
Gaspari, M., & Sądowski, A. 2017, ApJ, 837, 149
Ghirardini, V., Eckert, D., Ettori, S., et al. 2019, A&A, 621, A41
Gunn, J. E., & Gott, J. R. I. 1972, ApJ, 176, 1
Hirata, C., & Seljak, U. 2003, MNRAS, 343, 459
Hlavacek-Larrondo, J., McDonald, M., Benson, B. A., et al. 2015, ApJ, 805, 35
Hoffmann, K., Bel, J., Gaztañaga, E., et al. 2015, MNRAS, 447, 1724
Hoshino, H., Leauthaud, A., Lackner, C., et al. 2015, MNRAS, 452, 998
Hudson, D. S., Mittal, R., Reiprich, T. H., et al. 2010, A&A, 513, A37
Kaiser, N. 1984, ApJL, 284, L9
Kaiser, N. 1995, ApJL, 439, L1
Lacerna, I., & Padilla, N. 2012, MNRAS, 426, L26
Landy, S. D., & Szalay, A. S. 1993, ApJ, 412, 64
Lazeyras, T., Musso, M., & Schmidt, F. 2017, JCAP, 3, 059
Li, Y., Mo, H. J., & Gao, L. 2008, MNRAS, 389, 1419
Lin, Y.-T., Mandelbaum, R., Huang, Y.-H., et al. 2016, ApJ, 819, 119
Ludlow, A. D., Navarro, J. F., Boylan-Kolchin, M., et al. 2013, MNRAS, 432, 1103
Mandelbaum, R., Slosar, A., Baldauf, T., et al. 2013, MNRAS, 432, 1544
Mandelbaum, R., Tasitsiomi, A., Seljak, U., Kravtsov, A. V., & Wechsler, R. H. 2005, MNRAS, 362, 1451
Mao, Y.-Y., Zentner, A. R., & Wechsler, R. H. 2018, MNRAS, 474, 5143
McDonald, M. 2011, ApJL, 742, L35
McDonald, M., Allen, S. W., Bayliss, M., et al. 2017, ApJ, 843, 28

McDonald, M., Gaspari, M., McNamara, B. R., & Tremblay, G. R. 2018, ApJ, 858, 45

McDonald, M., Veilleux, S., Rupke, D. S. N., & Mushotzky, R. 2010, ApJ, 721, 1262

McDonald, M., Wei, L. H., & Veilleux, S. 2012, ApJL, 755, L24

McNamara, B. R., & Nulsen, P. E. J. 2007, ARA&A, 45, 117

McNamara, B. R., & Nulsen, P. E. J. 2012, NJPh, 14, 055023

Medezinski, E., Battaglia, N., Coupon, J., et al. 2017, ApJ, 836, 54

Miyatake, H., More, S., Takada, M., et al. 2016, PhRvL, 116, 041301

Montero-Dorta, A., Pérez, E., Prada, F., et al. 2017, ApJL, 848, L2

More, S., Miyatake, H., Takada, M., et al. 2016, ApJ, 825, 39

Murata, R., Nishimichi, T., Takada, M., et al. 2018, ApJ, 854, 120

Nakajima, R., Mandelbaum, R., Seljak, U., et al. 2012, MNRAS, 420, 3240

Navarro, J. F., Frenk, C. S., & White, S. D. M. 1996, ApJ, 462, 563

Niemiec, A., Jullo, E., Montero-Dorta, A. D., et al. 2018, MNRAS, 477, L1

O'Dea, C. P., Baum, S. A., Privon, G., et al. 2008, ApJ, 681, 1035

Oguri, M. 2014, MNRAS, 444, 147

Oguri, M., & Hamana, T. 2011, MNRAS, 414, 1851

Peebles, P. J. E. 1973, ApJ, 185, 413

Peebles, P. J. E. 1980, The Large-scale Structure of the Universe (Princeton, NJ: Princeton Univ. Press)

Pillepich, A., Porciani, C., & Hahn, O. 2010, MNRAS, 402, 191

Planelles, S., Fabjan, D., Borgani, S., et al. 2017, MNRAS, 467, 3827

Press, W. H., & Schechter, P. 1974, ApJ, 187, 425

Rasia, E., Borgani, S., Murante, G., et al. 2015, ApJL, 813, L17

Reid, B., Ho, S., Padmanabhan, N., et al. 2016, MNRAS, 455, 1553

Reyes, R., Mandelbaum, R., Gunn, J. E., et al. 2012, MNRAS, 425, 2610

Rossetti, M., & Molendi, S. 2010, A&A, 510, A83

Rozo, E., & Rykoff, E. S. 2014, ApJ, 783, 80

Rykoff, E. S., Rozo, E., Busha, M. T., et al. 2014, ApJ, 785, 104

Rykoff, E. S., Rozo, E., Hollowood, D., et al. 2016, ApJS, 224, 1

Salcedo, A. N., Maller, A. H., Berlind, A. A., et al. 2018, MNRAS, 475, 4411

Salomé, P., & Combes, F. 2003, A&A, 412, 657

Sato-Polito, G., Montero-Dorta, A. D., Abramo, L. R., Prada, F., & Klypin, A. 2019, MNRAS, 487, 1570

Sheth, R. K., & Tormen, G. 2004, MNRAS, 350, 1385

Simet, M., McClintock, T., Mandelbaum, R., et al. 2017, MNRAS, 466, 3103

Sinha, M., & Garrison, L. 2017, Corrfunc: Blazing Fast Correlation Functions on the CPU, Astrophysics Source Code Library, ascl:1703.003

Soares-Santos, M., de Carvalho, R. R., Annis, J., et al. 2011, ApJ, 727, 45

Sun, M. 2009, ApJ, 704, 1586

Sunyaev, R. A., & Zeldovich, Y. B. 1972, CoASP, 4, 173

Szabo, T., Pierpaoli, E., Dong, F., Pipino, A., & Gunn, J. 2011, ApJ, 736, 21

Thomas, D., Steele, O., Maraston, C., et al. 2013, MNRAS, 431, 1383

Tinker, J. L., Robertson, B. E., Kravtsov, A. V., et al. 2010, ApJ, 724, 878

Tremblay, G. R., Combes, F., Oonk, J. B. R., et al. 2018, ApJ, 865, 13

Truong, N., Rasia, E., Mazzotta, P., et al. 2018, MNRAS, 474, 4089

Villarreal, A. S., Zentner, A. R., Mao, Y.-Y., et al. 2017, MNRAS, 472, 1088

Voit, G. M., & Donahue, M. 2015, ApJL, 799, L1

Wang, H. Y., Mo, H. J., & Jing, Y. P. 2007, MNRAS, 375, 633

Wang, J., Navarro, J. F., Frenk, C. S., et al. 2011, MNRAS, 413, 1373

Wechsler, R. H., Bullock, J. S., Primack, J. R., Kravtsov, A. V., & Dekel, A. 2002, ApJ, 568, 52

Wechsler, R. H., Zentner, A. R., Bullock, J. S., Kravtsov, A. V., & Allgood, B. 2006, ApJ, 652, 71

Wen, Z. L., Han, J. L., & Liu, F. S. 2012, ApJS, 199, 34

White, S. D. M., & Frenk, C. S. 1991, ApJ, 379, 52

Yang, H.-Y. K., Gaspari, M., & Marlow, C. 2019, ApJ, 871, 6

Yang, X., Mo, H. J., & van den Bosch, F. C. 2006, ApJL, 638, L55

York, D. G., Adelman, J., Anderson, J. E., Jr., et al. 2000, AJ, 120, 1579

Zentner, A. R., Hearin, A. P., & van den Bosch, F. C. 2014, MNRAS, 443, 3044

Zhao, D. H., Mo, H. J., Jing, Y. P., & Börner, G. 2003, MNRAS, 339, 12

Zu, Y., Mandelbaum, R., Simet, M., Rozo, E., & Rykoff, E. S. 2017, MNRAS, 470, 551